ABSTRACT

Three-Dimensional Experimental Investigation of the Shape and Dynamics of a Rising Bubble in Stagnant Water with Particle Tracking Velocimetry. (December 1999)

Javier Ortiz-Villafuerte, B.S., Instituto Politécnico Nacional, México;

M.S., Instituto Politécnico Nacional, México

Chair of Advisory Committee: Dr. Yassin A. Hassan

The Particle Tracking Velocimetry technique has been used for a three-dimensional, transient, experimental study of a single bubble dynamics in a restricted medium. The three-dimensional velocity field was reconstructed via stereoscopic matching of two-dimensional images. A hybrid tracking technique has been used to determine the flow around a bubble. The development of the Shadow Particle Image Velocimetry allowed studying the bubble shape and rotation. An accurate estimate of the bubble dimensions, orientation, trajectory, and velocity and acceleration of a bubble rising in water, was obtained.

The flow around and within the wake of the bubble was determined from ensemble averaging instantaneous velocity fields. The ensemble average operation was performed by considering a conditional sampling technique. The conditional ensemble averaging was performed for specified bubble trajectories. It was found that bubbles rising close to the wall generate more turbulence, and the disturbances induced in the liquid reach further downstream, when compared to bubbles rising along the pipe core.

The bubble Reynolds number was in the range from 350 to 700. Regarding the bubble motion, it was found that the inclusion of the disturbed flow field in the bubble motion equation generates a scattering of the data for the drag and lift coefficients. The wall influence on these coefficients was introduced through the velocities and accelerations of the liquid and the bubble. The results indicate that the presence of the seed particles in the liquid have an influence on the bubble velocity and bubble shape. The instantaneous drag coefficient did not delineate a trend with respect to the rotation parameter; however, it shows a behavior similar to the standard drag

curve as function of the Reynolds number. The average drag coefficient values are 0.90 and 0.98 for the bubble trajectories along the pipe core and close to the pipe wall, respectively. No trend for the instantaneous lift coefficient values as a function of the Reynolds number and rotation parameter was observed. The average lift coefficient for the bubble trajectories rising along the pipe center and close to the pipe wall are of values of 0.37 and 0.44, respectively.

CHAPTER I
INTRODUCTION

Nuclear power plants have become more economically competitive, and the risk of severe accidents has significantly decreased, since safety issues have the highest priority. The new generation of light water reactors (LWRs), both pressurized water reactors (PWRs) and boiling water reactors (BWRs), have incorporated passive safety systems (Taylor 1989; Fisher 1990; Golay & Todreas 1990). These include gravity-driven cooling systems, and heat-removal from the reactor vessel through such physical processes as natural circulation, condensation, evaporation, etc. However, there is still a lack of knowledge of various phenomena occurring in the reactor, and the coupling relationships between nuclear and thermohydraulic parameters. Consequently, empirical or semiempirical correlations are still used to model some aspects of reactor behavior, in particular, when events involve two-phase flows. This approach is due to the lack of accurate expressions that exist to model the reactor under such conditions. In general, for accident analysis, computational codes give a reasonable representation of qualitative behavior, but the quantitative values may have high uncertainties. It is clear that energy, mass, and momentum transport and transfer between phases have to be investigated based on first principles.

The interaction between the two phases in a bubbly flow is a phenomenon not completely understood and still needs to be studied in detail. This particular flow is important not only in the nuclear industry, but also in the chemical, petroleum, and medical industries, among others. The turbulence phenomena in bubbly flow regimes needs to be better understood to improve predictions of the flow behavior and the heat and momentum transfer characteristics. A clear understanding of these physical processes has a direct impact in developing and improving many engineering systems.

For dilute bubbly flows, in which bubble interaction is at a minimum, the turbulent motion of the liquid generated by the bubble is yet to be completely understood. Dilute bubbly flows are an extension of a single bubble dynamics. Therefore, improvements in the description and modeling

---

This dissertation follows the style and format of the *International Journal of Multiphase Flow*.

of a single bubble motion, the flow field around the bubble, and the dynamical interactions between the bubble and the flow will consequently improve bubbly flow modeling. The understanding of the physical phenomena will have far-reaching benefits in upgrading the operation and efficiency of current processes and in supporting the development of new and innovative approaches.

Most of the work performed in single bubble dynamics study does not consider the wall influence on bubble motion and shape. In many practical applications, such as steam generators, pressurizers, and nuclear reactor fuel bundles, bubbles rise in narrow spaces, where the solid structure influence cannot be ignored. The need of studying the influence of wall on bubble rise velocity, shape, drag, mass and lift coefficients is apparent.

Some of the results and references related to the work to be developed in this investigation are presented in the following sections. This chapter closes presenting the objectives and questions to be answered in this experimental study. An overview of the next chapters is also included.

1.1. Bubbly flow studies

Many theoretical, numerical, and experimental investigations about two-phase bubbly flows exist in the scientific literature. They cover a wide range of subjects, such as single bubble and droplet dynamics, turbulent bubbly flow calculations, heat and mass transfer, bubbly flow modeling, etc.

The mathematical modeling of the two-phase flow equations of mass, momentum, and energy has been presented by Ishii (1975), Drew (1983), Kashiwa & Gore (1991), Drew & Passman (1999), among other authors. Wijngaarden (1976) studied the interaction between bubbles in liquid. Biesheuvel & Wijngaarden (1984) derived equations of mass and motion for dilute bubbly flow. Kataoka *et al.* (1998) determined the turbulence spectrum in bubbly flow. They found that the turbulence spectra in the inertial sub-range is proportional to –8/3 power of the wave number, compared to the –5/3 power for single phase. This result is in agreement with experimental data by Lance & Bataille (1991).

It is now well known that the void fraction (the ratio of the volume of the dispersed phase to the volume of the dispersed phase plus the continuous phase volume) peaks near the wall in co-current flow, for low void fraction. As the void fraction increases the transition from bubbly to

slug flow occurs, and then the void fraction peaks in the center, although smaller peaks close to the wall still occur. Void coring also happens in counter-current flow. It is also known that bubbles of less than about 3 or 4 mm of equivalent diameter travel close to the container wall, while bigger bubbles tend to rise along the center (Tran-Cong *et al.* 1998). These phenomena of phase distribution have been associated with turbulence in the liquid phase, and with the lift forces acting on the bubbles. The phase distribution phenomena have been studied by Drew and Lahey (1982), Žun (1988), Lahey (1990), and Lopez de Bertodano *et al.* (1990), among others.

The study of the turbulence structure in a two-phase bubbly flow is one of the problems in which experimental, numerical and theoretical work is being extensively done nowadays. It is now considered that the turbulence in two-phase flow has two different sources: one is the turbulence generated in the continuos liquid phase, and the other is the turbulence induced by the movement of the bubbles in the flow. This last agitation due to the bubbles has been called pseudo-turbulence (Lance & Bataille 1991). Understanding of bubble-induced turbulence is still lacking. For homogeneous potential bubbly flows, the Bieshevel & Van Winjgaarden's (1984) results for the pseudo-turbulence stress tensor are widely used.

Theofanous & Sullivan (1982) measured turbulence in dispersed two-phase bubbly pipe flow. They also proposed a relationship to predict turbulence levels. In other experimental investigation, Liu & Bankoff (1993) found that under certain conditions, bubbles present in the flow could reduce the fluid turbulence to a lower level than that corresponding to a single-phase flow. These researchers detected this phenomenon at high liquid flow rates and low void fractions. In turbulent bubbly flows, bubbles modify both production and dissipation of turbulent kinetic energy (Serizawa *et al.* 1975; Wang *et al.* 1987; Besnard *et al.* 1991; Kataoka & Serizawa 1991; Liu & Bankoff 1993; Kataoka *et al.* 1993; Nakoryakov *et al.* 1996). Serizawa & Kataoka (1994) have proposed a bubble exchange model to predict the turbulent momentum transport term associated with bubbles. Bubble wakes transport some turbulent kinetic energy to the liquid (Morel & Bestion 1997).

1.2. Single bubble dynamics

Most of the two-phase bubbly flow systems employed in industry consist of bubbles rising in swarms. Considering the dynamics of a single bubble and its associated wake, however, can make a first approach to the complex interaction phenomena between bubbles and wakes. This is so because many of the assumptions made in the modeling of two-phase flow are directly related

to phenomena involving single bubbles. Frequently, drag, added mass, and lift coefficients used in bubbly flow analysis are those measured or computed for single bubbles. The need of information about parameters for single bubbles then becomes apparent.

Clift *et al.* (1978) presented a complete summary of hydrodynamic information from experimental, theoretical, and numerical studies about single particles (bubbles, drops, or solid particles). Heat and mass transfer data were also presented. For fluid particles, the measurements and correlations of terminal velocities in pure and contaminated systems, the formation and shedding of wakes in the surrounding fluid, and the internal circulation in the particles were discussed. Furthermore, particle behavior in turbulent flows, unsteady analysis of particle motion, and formation and breakup of fluid particles were also considered. Fan & Tsuchiya (1990) presented a review of hydrodynamics of bubbles. They addressed the phenomena associated with bubble wakes in liquids and liquid-solid suspensions. Results from theoretical, numerical, and experimental studies were shown. Further, the authors described the phenomena associated with wakes for spherical-cap bubbles. Crowe *et al.* (1998) presented the multiphase phenomena from both Eulerian and Lagrangian approaches, for single and groups of particles. These researchers presented methods to numerically solve the conservation equations.

Although the three references just mentioned summarize most of the work done on single particles, many questions remain unanswered and more investigations are being performed. The equation of motion for single particles presents the problem of accurately describing the forces acting on the particles. Even for small spherical particles moving on rectilinear paths, the question of including or not, and how to include, unsteady forces in the motion equation is unclear. Michaelides (1997) presented a review of transient equation of motion for particles. It is generally accepted that the Basset or history force is negligible in gas-liquid systems for Reynolds (Re) numbers higher than about 100 (Park *et al.* 1995; Domgin *et al.* 1998). Park *et al.* (1995) found that both steady and unsteady forces cannot be accurately predicted in contaminated systems. A similar problem occurs during the measurement of the drag coefficient. In fact, the cause of the discrepancies found in the literature for drag coefficient of bubbles rising in stagnant water is considered due to different levels of contaminants in the water.

Lift coefficients are difficult to measure and compute because the lift force is usually smaller than the drag force acting on a bubble (Sridhar & Katz 1995; Takagi & Matsumoto 1998). For bubbles at high Re, the commonly used value of the lift coefficient is 0.5. This value is obtained using potential flow theory. Magnaudet *et al.* (1995) found that the same value of 0.5 for the lift

coefficient can be used too in an accelerated flow. However Kurose *et al.* (1998) claimed that the lift coefficient strongly depends on the shear rate. This is contrary to Magnaudet *et al.*'s result. Recently, computations of the lift coefficient in a turbulent boundary layer by Tran-Cong *et al.* (1998) showed values up to about 3.5.

Regarding the flow surrounding a bubble, Miksis *et al.* (1982) computed the bubble shape and the surrounding fluid flow field. They considered potential flow and high Re, so the viscosity effects are restricted to the boundary layer of the bubble. A reformulation of the motion equations as an integro-differential system of equations was derived. Ryskin & Leal (1984) considered a similar problem, but they also included a study of flow separation at the bubble surface. They solved the system of equations with a finite-difference scheme, and for Re from 1 to 200, and Weber (We) numbers up to 20. They concluded that the onset of flow separation depends generally on both Re and We. Tomiyama's group (Tomiyama 1998) and Tryggvason's group (Esmaeeli & Tryggvason 1999) have considered computations for single bubbles and arrays of bubbles. Tsuchiya & Fan (1988) have carried out experimental studies of the wake for spherical-cap bubbles. Lunde & Perkins (1997), Hassan *et al.* (1998) and Brücker (1999), among others, studied the wake of ellipsoidal bubbles.

The pseudo-turbulence generated by single bubbles has been investigated by Hassan *et al.* (1998), Ellingsen & Riso (1998), Rivière & Cartellier (1998) and Suzuki *et al.* (1999). Suzuki *et al.* (1999) also presented a correlation for the size of the boundary layer of a bubble. Hassan *et al.* (1998) also performed a transient study of the measured kinetic energy within the test volume. The measurements were carried out in a small-diameter pipe, consequently, wall influence was noticeable.

1.3. Bubble shape analysis and three-dimensional reconstruction

Bubble shapes and sizes, and their variations, are important parameters. They reflect the dynamic evolution of the gas/liquid interface due to the pressure changes of the bubble and the surrounding fluid. Moreover, the interfacial area is an important parameter for heat and mass transfer between bubbles and the surrounding fluid. The interfacial area values are determined by knowing the bubble surface shape and bubble dimensions. A bubble's rise velocity and path are known to be dependent on its shape and dimensions.

Clift *et al.* (1978) presented a generalized graphical correlation of fluid particle shapes, in terms of the Eötvös (Eo), Morton (M), and Re dimensionless numbers. Furthermore, wall effects

on the motion and particle shape were also considered. Bhaga & Weber (1981) studied shapes and terminal velocities of bubbles rising in viscous liquids. They also presented a graphical correlation for the shape of fluid particles similar to that one of Clift *et al.* (1978). Fan & Tsuchiya (1990) discussed characteristics of rising bubbles, such as shape, terminal velocity, drag, paths, orientation, and effects of wake on bubble motion. Karamanev (1994) has proposed a semianalytical equation describing the single bubble rise velocity in a quiescent, contaminated liquid for any shape and size of a bubble. Karamanev's equation requires that the internal circulation has no effect on the rise velocity, and that the drag coefficient of the bubble can be computed on basis of its real shape and size. Kataoka & Serizawa (1990) performed measurements of interfacial area concentration. In their study, they derived an equation relating bubble diameter to the interfacial area concentration. Kataoka *et al.* (1986) found that the interfacial area concentration has a peak near the wall in bubble flow, consistent with the results for void fraction.

Among many numerical studies of bubble shape and motion, Tomiyama *et al.* (1993) considered bubble motion in stagnant liquid as a function of M and Eo numbers. Their two-dimensional results for bubble shape showed similar shapes to Clift *et al.*'s (1978) three-dimensional graphical correlation. Manga & Stone (1995) studied the deformation caused by hydrodynamics interactions between bubbles. Takagi & Matsumoto (1998) performed a study of the forces acting on the bubble. The study of bubble trajectory has been experimentally considered by Saffman (1956), Mercier *et al.* (1973), Lunde & Perkins (1997), and Brücker (1999), among others.

The shape of an object boundary contains important information. For example, shapes of fluid particles reflect the dynamic interactions between the fluid particle and its surrounding environment. Several methods exist to detect or identify and, if necessary, reconstruct object shapes. Moreover, if its shape can identify an object, it is much easier only to store and work with its boundary. Geometric curves and surfaces are widely used in computer, robot, or machine vision for object recognition, since many objects are combinations of such geometric models. For arbitrary shapes, parametric curves are also used for identification and reconstruction processes. For example, Bezier and spline curves are well known. Recently, rational Gaussian curves and surfaces have attracted attention (Goshtasby 1993). Another detection method maps the original shape into a parametric space. A good example of this method is the Hough transform. The Hough Transform (HT) is a method to identify curves by

exploiting the duality between points on a curve and the parameters of such a curve (Ballard 1981). The HT decomposes a boundary into its constituent shape primitives. These primitive curves have associated parameters, which are used to build a symbolic representation of the shape under identification (Leavers 1992).

Shape detection of fluid particles is often performed by visual inspection of photographic plates, since the resolution of the photographic film is much higher than digital recording systems. For the latter, image processing is a tool to improve the resolution of the image. Computer vision techniques, such as thresholding, noise removal, edge detection, etc., are part of the image processing. Ellis *et al.* (1992) used image processing to measure the geometry of hydrogen bubbles and their dynamic growth. To determine the overall shape of the bubbles, they used a fifth-order Bezier curve.

In three-dimensional PIV measurements, a bubble image could show only fragments of the bubble, and not the whole two-dimensional shape, and/or show up a different shape from the actual one. For such cases, it is clear that a reconstruction process is necessary. Even when the two-dimensional shape is well defined, parameters such as orientation and dimensions still need to be computed. Shadow techniques satisfy the need of acquiring the whole two-dimensional shape of an object. For an air-water system a Shadow Particle Image Velocimetry (SPIV) provides an image of the shadow of the whole air bubble, in a plane, which can be combined with images from other cameras to determine the three-dimensional shape and dimensions of the bubble.

Most of the implementations of HT involve straight-line detection. When the object to be recognized and reconstructed is symmetric, for example circles, ellipses, etc., the dynamic generalized Hough transform (DGHT) algorithm (Leavers 1992) has been proven to be particularly useful. Although not always direct, all the parameters associated with a curve are easily computed with the DGHT algorithm. For an ellipse, the DGHT will determine the center of coordinates, the angle of rotation, and the value of the two semiaxes. This algorithm, further, can be used when occlusion of objects appears on the image. For distorted images of the bubble, the DGHT algorithm can be used to reconstruct first a two-dimensional shape, and then, through stereo matching with an image from another camera, the three-dimensional shape of the bubble.

1.4. Three-dimensional particle image velocimetry and tracking algorithms

Analytic and numeric solutions to the conservation laws are generally restricted to ideal flows and simple geometry, due to the nonlinearity of the equations, the complex interactions between phases, and the lack of accurate closure relationships. Therefore, it is readily apparent that there is a need for accurate experimental measurements that provide data for bubbly flows. This information is useful for testing new theoretical models, and developing or improving existing computer constitutive models.

It is well known that turbulent flows are three-dimensional. For two-phase flows, the interaction between phases is also three-dimensional. Consequently, any flow measurement technique considered for two-phase flow investigations has to be able to simultaneously determine the three velocity components. Ishii & Theofanous (1998) have edited a special issue about some advanced experimental techniques currently employed for two-phase phenomena investigation.

In single bubble dynamics and dispersed bubbly flows, the velocity fields contain many different velocity scales. For example, just in front of the bubble, the liquid velocity is of the same order of magnitude as that of the bubble. In regions several bubble diameters away from the bubble, however, the liquid velocity field may not detect or feel the influence of the presence of the bubble. The various time and length scales involved in single bubble dynamics imply that full-field information is needed to observe the flow behavior. Point measurement techniques can provide information at various time scales, but their spatial resolution is limited. On the other hand, flow visualization measurement techniques can provide information at any point in the measurement zone. However, with present electronic technology, the duration of the measurement is limited due to requirements for large storage and fast data handling.

Particle image velocimetry (PIV) is a nonintrusive flow measurement technique that yields a two-dimensional velocity field. This technique is a very efficient tool since it can obtain both qualitative and quantitative spatial information about the flow being studied. Transient information is also available since a series of pictures of the same area under study can be taken in a very short time. In recent years, PIV has become a standard tool for fluid mechanics studies, and the number of papers in which this technique is used has grown exponentially. Reviews about PIV techniques have been presented by Adrian (1991), Buchhave (1992) and Grant (1997). Grant (1994) edited a special issue about selected papers on PIV.

Particle image velocimetry has been extended for three-dimensional measurements. Images from at least two cameras are acquired. Then a stereo pair matching method is performed to determine the three-dimensional position of a fluid particle in the viewing volume under study

(Kasagi & Nishino 1991; Maas *et al.* 1993; Prasad & Adrian 1993; Costes *et al.* 1994; Hassan *et al.* 1998). A three-dimensional reconstruction from orthogonal views was performed by Adamczyk & Rimai (1988). For multiphase investigations, PIV can also be used if the different phases can be distinguished. Philip *et al.* (1994) used fluorescent seeds and special filters, by letting one camera to capture both phases and other camera in conjunction with the filter only capture the fluorescent seed images. Hassan *et al.* (1998) also differentiated between the phases by simply considering the size of the images.

With PIV, the velocity is measured by recording the displacement of microscopically small neutral density particles. Two or more short light pulses fired with a known time separation illuminate these tracer particles, embedded in a volume of the flow. The images appear with spacing proportional to the local velocity vector. The problem, then, is to track and extract the velocity information quickly and accurately from the pattern. Different tracking methods may be used to process the data. These include techniques such as cross-correlation (Hassan *et al.* 1992; Yamamoto *et al.* 1995), particle tracking velocimetry (Nishino *et al.* 1989; Malik *et al.* 1993; Wernet and Pline 1993), Spring Model (Okamoto *et al.* 1995), etc. Recently, new algorithms based on pattern recognition are becoming popular; among them neural networks, genetic algorithms, and fuzzy logic techniques seem to have good potential for particle tracking. There are different kinds of neural networks (NN) used in PIV. Grant & Pan (1995) used Kohonen algorithm, while Hassan & Philip (1997) used an Adaptive Resonance Theory (ART2) technique. Yoon *et al.* (1997) employed a genetic algorithm for particle tracking. Fuzzy Logic techniques have been employed by Wernet (1993).

1.5. Objectives

The purpose of this investigation was to provide experimental data of the shape and dynamic behavior of a single bubble rising in stagnant water in a small-diameter pipe. The interaction of the bubble with its surrounding fluid was studied. The structure of the wake flow was also investigated. Ensemble averages under the condition of what trajectory the bubble follows in its rising path were used to determine mean quantities. Fluctuating components were obtained by Reynolds decomposition.

Some of the questions that this experimental investigation tries to answer are:

- how much energy the bubble brings into the test zone,
- how long it takes the viscosity and wall friction to dissipate the energy in the test volume,

- how much turbulence the bubble induces,
- how the structure of the bubble wake is,
- how far upstream and downstream the bubble-induced liquid agitation is felt,
- what the magnitude of the different forces acting on the bubble is, and
- what the pipe wall influence on drag and lift coefficients is.

The overview of the following chapters is next. In Chapter II, the experimental setup and the camera calibration procedure are presented. Chapter III shows the application of the hybrid tracking technique, which is a combination of the ART2 NN and Spring Model. This approach increased the number of velocity vectors, and the determination of the three-dimensional position of the tracer particles through a stereoscopic technique. The implementation of the SPIV technique and its application for bubble shape identification is presented in Chapter IV. The description of the DGHT algorithm for two-dimensional bubble shape reconstruction for both PIV and SPIV images, and the combination of the bubble parameters to determine the three-dimensional shape of the bubble are also shown in Chapter IV. In Chapter V the description of both the mean and turbulent flow field upstream and downstream the bubble is shown. The wake structure is also analyzed in this chapter. An uncertainty analysis of the measured velocity field is also presented in Chapter V. The forces acting on the bubble and the determination of drag and lift coefficients are shown in Chapter VI. Also, Chapter VI presents an analysis of the bubble shape. Finally, Chapter VII presents a summary of this experimental investigation, the conclusions, and recommended future work.

CHAPTER II
EXPERIMENTAL SETUP AND CAMERA CALIBRATION

An experimental facility was constructed to conduct measurements of the interaction between a rising air bubble and its surrounding fluid in a pipe flow. The experimental set up consisted of a flow system, an optical system, and a data acquisition system. All these are described in detail next. Then the mathematical model used to calibrate the cameras is described. The uncertainties associated with the calibration process are presented.

2.1. *Experimental setup*

A schematic of the experimental setup and the camera configuration is shown in figure 1. Air bubbles of average size 3-mm spherical-equivalent diameter were injected into a 12.7-mm i.d., 15.9-mm o.d., 1.3-m long Plexiglas pipe. The flow was seeded with small polystyrene tracer particles. The density of these particles is 1.05 g/cm^3 and their diameter is 40 μm. The particles need to be small enough to effectively follow the flow, and large enough to reflect a sufficient amount of light to be detected by the cameras. Throughout the measurements, it was assumed that the tracer particles are homogeneously distributed over the whole viewing volume, including those regions close to the pipe wall. This could be confirmed by observing the distribution of the particle images in the viewing volume. The measurements were carried out at a location of about $L / D = 66$, where L is the length from pipe inlet to measurement zone, and D the pipe inner diameter. In general, bubble terminal velocity is reached just a few bubble diameters after bubble release. In the case of this experimental study, once the bubble reached the viewing volume it would have gained a velocity equal to the terminal velocity. However, under certain conditions, such as unsteady, non-uniform flows, bubble terminal velocity may not reach steady state.

A water filter removed any contaminants exceeding a diameter of 5 μm, prior to the commencement of the experiment and the addition of the tracer particles. Enclosing the test section in a rectangular Plexiglas box filled with water, see figure 1a, reduced the pipe curvature effect. The Plexiglas box has the same refractive index as that of the pipe. In addition, as explained later, refraction effects were included in the calibration parameters.

The optical elements of the set up included an argon ion laser, an acoustic optic modulator

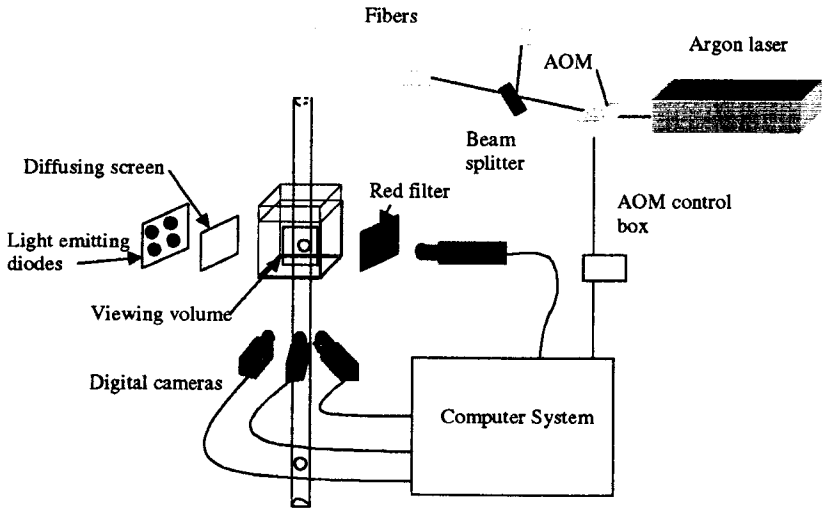

(a)

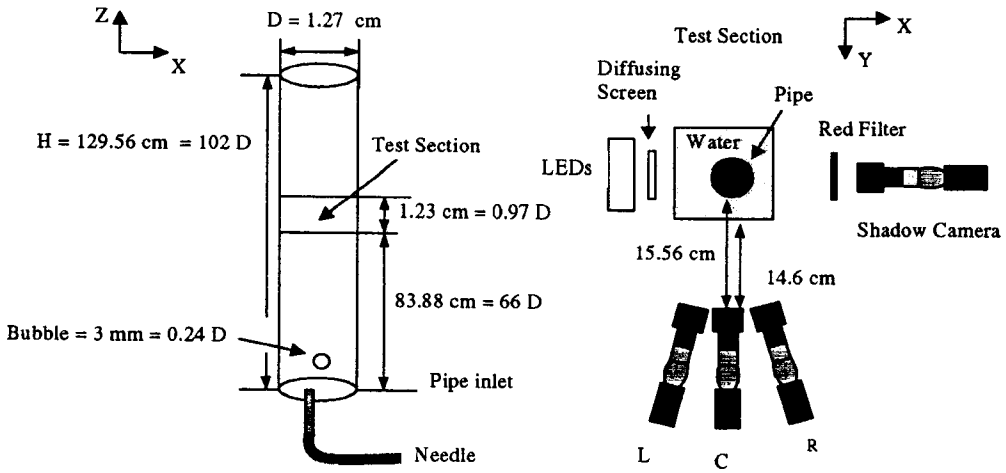

(b)

Figure 1. a) Facility setup and camera configuration; and b) some relevant dimensions are shown.

(AOM), a beam splitter, mirrors, and a multimode fiber with a fiber coupler. The light source was the argon ion laser. It has a maximum power output of 5 W, comprising 7 frequency groups. The 514-nm frequency was selected for illumination because it delivered the maximum power output (about 2 W). This frequency corresponds to green light. The laser beam passed through the AOM (its rise time is less than 200 ns), which chopped the continuous laser light at intervals of 16.67 ms. The laser pulse width was 250 μs. Then, the light was directed to a beam splitter, which divided the beam into two parts. Each part was directed to a separate fiber coupler. The light beam was transmitted to the viewing volume through two 400-μm i.d. multimode fibers. These two fibers were placed at the top of the tube to illuminate the viewing volume with cones of light. The images (size, intensity, and distribution on the image) of the tracer particles indicated that the viewing volume was adequately illuminated. Four Charged Couple Device (CCD) cameras were utilized in this experimental investigation. As shown in figure 1, one of the cameras was only used for bubble shape analysis. For this analysis, forward scattering was utilized. Light Emitting Diode (LED) units emitting red light coupled with a diffusing screen were used to illuminate the test volume. A red filter was placed in front of the Shadow camera to detect the red light images only.

Several optical elements were attached to the CCD cameras to improve the accuracy of the measurements. Such attachments were: a close-up lens, a telephoto lens, a 15-mm extension ring, a 2× range extender, an intensifier tube, a 25-mm lens, and a 10-mm extension ring. The close-up lens was mounted on the front of the telephoto zoom lens. This is a macro zoom lens of focal length 18-108 mm, *f* 2.5. The purpose of adding the close-up lens and the 2×-range extender was to enlarge the magnification factor of the whole lens assembly. The 15-mm extension ring adjusted a focused image through the lens onto the intensifier tube. The 10-mm extension ring focused the image produced by the intensifier tube onto the camera's CCD detector array. The intensifier tube is encapsulated in a protective case, and is operated by a 3 V DC. It has a glass window, and contains a high-efficiency GaAs photocathode with a luminous gain of 12000. Both gain and brightness of the intensifier can be adjusted for better performance. The whole camera assembly can be seen in figure 2.

The CCD cameras have a resolution of 640×480 pixels, when run in the RS-170 frame interlace mode at 30 frames/s. By running the cameras in field mode, the resolution is reduced by half in the CCD array Y-direction. Thus, the camera's resolution is only 640×240 pixels; however, the framing rate is doubled to 60 frames/s. The cameras were run in field mode to take

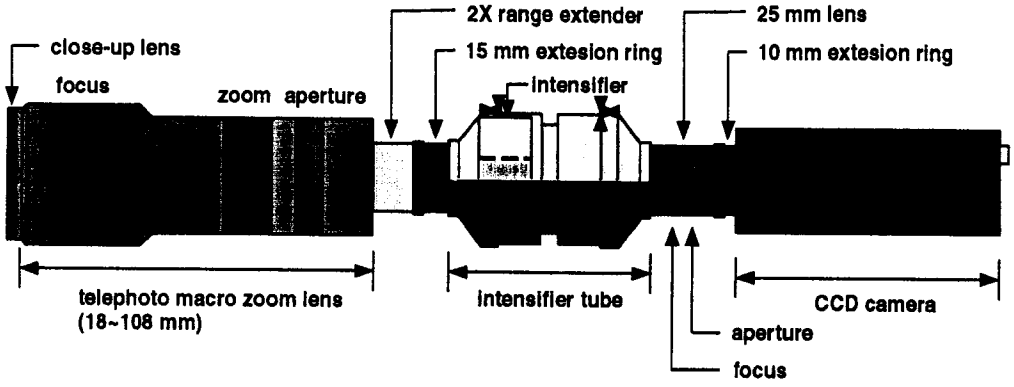

Figure 2. Camera assembly.

advantage of the higher framing rate, therefore allowing for the study of higher velocity flows. The inclusion of an image intensifier did not deteriorate the resolution of our images because the image intensifier has at least 2 million microchannels, where the incoming light rays increase their intensity, and its output format (2/3") is bigger than our 640×480 CCD array (8.64 mm × 6.48 mm). When the cameras are run in field mode there are odd and even fields. However, the particle image sizes were, in average, approximately 10 pixels in area, and only the centroid of individual particle images are used for the tracking process. The effect of the 1-pixel difference from odd and even lines, then, falls within the calibration error, as explained later.

Once the cameras were triggered, the images were exposed onto the CCD array, and simultaneously stored in 4 frame grabber boards, also called imaging boards, installed in two personal computers (2 imaging boards per computer). Each imaging board is able to store up to 4 megabytes of data, or equivalently 27 sequential image frames. These 27 frames, from each camera, were then transferred to the computer's hard drive. Then all the sets of 27 frames were transferred to workstations, where the data analysis was performed. The imaging boards had also the function of controlling all the signal system: timing of laser pulses, camera triggering, and data acquisition.

2.2. Camera calibration

Camera calibration is the technique from which camera parameters are determined, by using set of image points with known world coordinates. Such parameters include camera position in

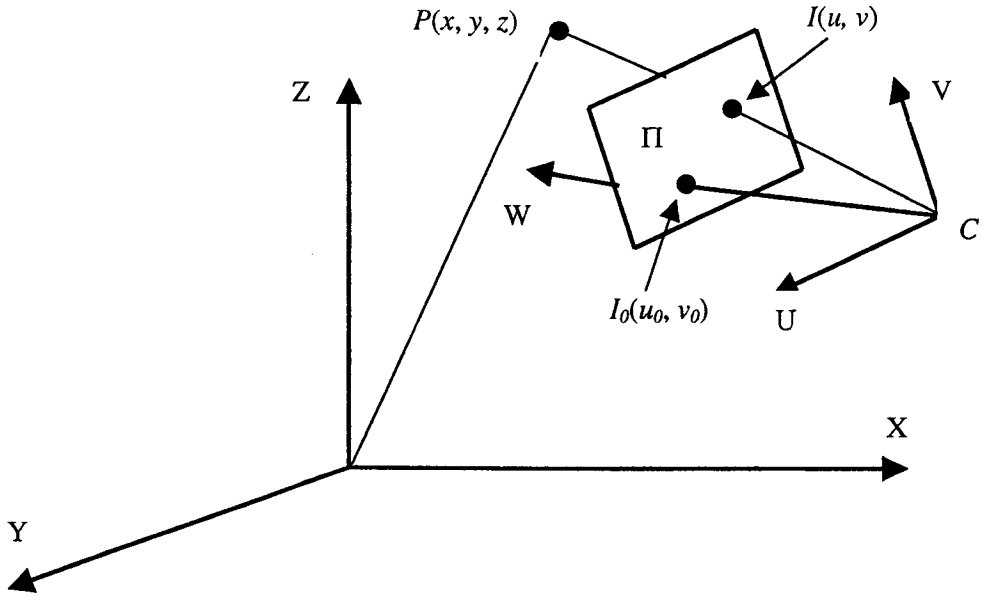

Figure 3. The pinhole camera. A point *P* in the 3D world coordinate system is projected into an image point *I*, located at the interception of the line joining the point *P* and the camera center of projection *C* through the camera image plane Π.

the world coordinate system and orientation. Also, internal camera parameters, such as focal length, or principal point distance, lens distortion parameters, etc. can be computed through camera calibration.

2.2.1. The pinhole camera model and the direct linear transformation method

In order to construct a mathematical model relating the image points and the three-dimensional world positions of an object, a camera model is needed. One of the most widely used camera models is the so called *pinhole* model, in which the camera is modeled by its optical center, or principal point, *C* and its image plane Π, see figure 3. The pinhole camera is an idealized device for describing the light rays passing through the camera optical center, or center of projection, and falling into a solid angle determined by the camera image plane. Now, since light travels along straight lines, each image point corresponds to a well defined light ray passing

through the pinhole, and coming from an object in the three-dimensional world. This transformation of a three-dimensional (3D) world point into a two-dimensional (2D) image is known as perspective projection.

Although perspective projection is non-linear, a series of linear transformations can relate a point P of world coordinates (x, y, z) to an image point I of coordinates (u, v), if projective coordinates are used. The linear transformations consist of translation and rotation of the projective center of the camera as a rigid body, followed by a perspective transformation (Gonzales & Wintz 1987; O'Hern *et al.* 1997).

Let $I^* = (s\,u, s\,v, s)^t$ be the projective coordinates of I, and $(x, y, z)^t$ be the coordinates of P, then we can write

$$\begin{bmatrix} s\,u \\ s\,v \\ s \end{bmatrix} = \mathbf{T} \begin{bmatrix} x \\ y \\ z \\ 1 \end{bmatrix}, \qquad [1]$$

where $\mathbf{T}$ is a 3×4 matrix, generally called the perspective matrix. $\mathbf{T}$ is defined up to a scale factor, so it needs a constraint to be specified uniquely. The simplest constraint is to set one of the $\mathbf{T}$ elements to a constant different that zero. In the particular case that P is in the focal plane of the camera, that is, the line CP is parallel to the image plane Π, $s = 0$ and then the image coordinates are undefined.

Equation [1] can be rewritten in its components to arrive to a relationship between image and world coordinates for a given point as:

$$u = \frac{t_{11}x + t_{12}y + t_{13}z + t_{14}}{t_{31}x + t_{32}y + t_{33} + 1}, \qquad [2]$$

$$v = \frac{t_{21}x + t_{22}y + t_{23}z + t_{24}}{t_{31}x + t_{32}y + t_{33} + 1}, \qquad [3]$$

where it was assumed $s \neq 0$, and set $t_{34} = 1$.

Equations [2] and [3] simply, implicitly, reflect the collinearity condition, which states that

the point P, its corresponding image point I, and the camera center of projection C lie on a straight line. Thus, they do not consider the refraction effect, when light ray travels through different physical media, neither any kind of lens distortion, and image digitization effects, if electronic equipment is used in the acquisition and storage of the images (Maas *et al.* 1992; Maune 1975). Equations [2] and [3] have 11 unknowns, combined, so at least six non-coplanar image-point coordinates and their corresponding world-point coordinates are needed to solve for the eleven t_{ij}'s. Once the latter are computed, all camera parameters can be determined, although the equations to solve will be non-linear.

Equations [2] and [3] are the same derived by Abdel-Aziz & Karara (1971). These equations are denoted as the Direct Linear Transformation (DLT) method. When the DLT method was refined to allow for the computation of lens distortion parameters, film deformation, etc., it still was referred as DLT (Marzan & Karara 1975). Based on Marzan and Karara's experimental investigations and those from other researchers (Bopp & Krauss 1978; Karara 1980), it was found that in most cases only the first radial distortion coefficient was needed to model lens distortion and film deformation effects. The inclusion of the first radial distortion coefficient κ in [2] and [3] is as follows:

$$u + (u - u_0)\kappa r^2 = \frac{t_{11}x + t_{12}y + t_{13}z + t_{14}}{t_{31}x + t_{32}y + t_{33} + 1}, \qquad [4]$$

$$v + (v - v_0)\kappa r^2 = \frac{t_{21}x + t_{22}y + t_{23}z + t_{24}}{t_{31}x + t_{32}y + t_{33}z + 1}, \qquad [5]$$

where u_0 and v_0 are the image coordinates of the center of projection, and $r^2 = u^2 + v^2$. This system of equations can be solved by a non-linear least squares method, or by iteration. Again, at least six non-coplanar image-point coordinates and their corresponding world-point coordinates are needed to solve for the twelve unknowns, the eleven t_{ij}'s and κ.

2.2.2. Calibration data

One of the major problems on calibration is that of the different physical media through which the light rays travel in an actual experimental set up. When all of the surfaces to be crossed, from one medium to other, by a ray of light are planar, a mathematical model similar to

that used by Maas *et al.* (1992) can be implemented. For curved surfaces, however, the problem is much more complex, since the normal to such surfaces changes at every surface point, in the most general case. Specifically for pipe geometry, the normal is a function of the angle of the incident ray. Then, the equations describing the collinearity condition should be extended to consider the change of refraction index for different physical media.

Some alternatives exist to reduce the refraction effect, overall for curve surfaces. For example, the use of liquids with refraction index close to, or same as, that of a thin-wall container of the fluid under research, has been used to help to reduce, and sometimes minimize, the refraction effect (Chen & Fan 1992).

Instead of extending the model for the collinearity condition, some researches have preferred the option of calibrating under the same conditions in which the actual experiment would be carried out (Tsao *et al.* 1995; Hassan *et al.* 1998). In this way, the refraction effects are included into the eleven transformation coefficients of the DLT method. This alternative presents the problem of constructing a test, or calibration, set up which must be placed exactly on the same position where the actual experimental set up would be located.

In this experimental investigation, a rigidly supported tank full of water was used to maintain the pipe on a fixed position. The tank had two circular holes, one at the bottom and one at the top, of the same outside diameter of the pipe, see figure 1a. Since the tank could not move, and the pipe had to go through the two holes, other pipe of the same dimensions and material could be used as test set up, and then the transformation coefficients t_{ij}'s, and κ if used, computed so, could be used for the actual experimental data. The test pipe was also full of water to accurately simulate the actual experimental conditions.

The calibration procedure started with setting a coordinate system. Then a calibration grid was constructed by printing tiny circular black dots of 0.2 mm of diameter on a sheet of paper. The dot pitch was 1.27 mm on both horizontal and vertical directions. The calibration grid had a total of 24 dots, arranged in a matrix-like pattern of 3 columns and 8 rows. The grid was glued to a thin plastic slab, which could be moved forwards, backwards or sideways by a micrometer. The accuracy of the movement of the micrometer is less than 0.01 mm.

Then, the approximate location of the center of the pipe was achieved by using the views of the two orthogonal cameras, the Center and the Shadow cameras, according to the notation used in figure 1. The Center camera was that seeing the XZ world plane, and the Shadow camera was that seeing the YZ world plane. To determine the center of the pipe on the images of these two

cameras, it was first necessary to obtain the location of the pipe walls on the images. Due to the very high zoom of the camera lens used in this experiment, the dot pitch distances were basically constant across the pipe images, and then the middle point between the wall positions it was considered to be the center of the pipe on each respective world plane. The calibration grid was placed such that the center column coincides with the pipe center on the XZ plane, and the front of the slab was at the center of pipe on the YZ plane.

Once the origin of coordinates was set, the calibration grid was moved forwards 8 times, at intervals of 0.5 mm each time. Then, the grid was repositioned at the origin, and then moved backwards 5 times at intervals of 0.5 mm too. At some positions close to the center of the pipe, the calibration grid was moved sideways, once to the left and once to the right, 1.27 mm (one dot pitch distance). For each of all positions of the calibration grid, images were taken with all 4 cameras (obviously, the shadow camera only sees the edges of the calibration grid, so only the Y world direction can be calibrated in this way) used in the experiment. In this way, calibration data all over the viewing volume were gathered. A total of 624 calibration points (26 images) were acquired, but due to a digitization problem in one of the cameras, the images of top row of the calibration grid was not considered, and then 546 points were actually used as calibration data.

Figure 4 shows the 4 images, one from each camera, of the calibration grid, when the grid was placed at the origin. The images have been negated and enhanced for better visualization. The average area of a calibration point is about 70 pixel.

2.2.3. Computation of transformation coefficients

Once all the calibration images were acquired, they were fed into a computer program that determined the centroid of the calibration spots. The program is called FINDSPOTS, and it is written in FORTRAN 77 (Blanchat 1992). The program computes the spot centroid to subpixel accuracy, by calculating the area of the spots that surpass a predetermined gray-level threshold. The output of the program is the u and v coordinates of the centroid of the calibration points, which along with their corresponding world coordinates provide the necessary information to compute the transformation coefficients.

To compute the transformation coefficients in [2] and [3], this system of equations was set in matrix form. The system was solved by the subroutine DGLSS, which is part of NETLIB. NETLIB is a software repository, freely available through internet, and it is maintained basically

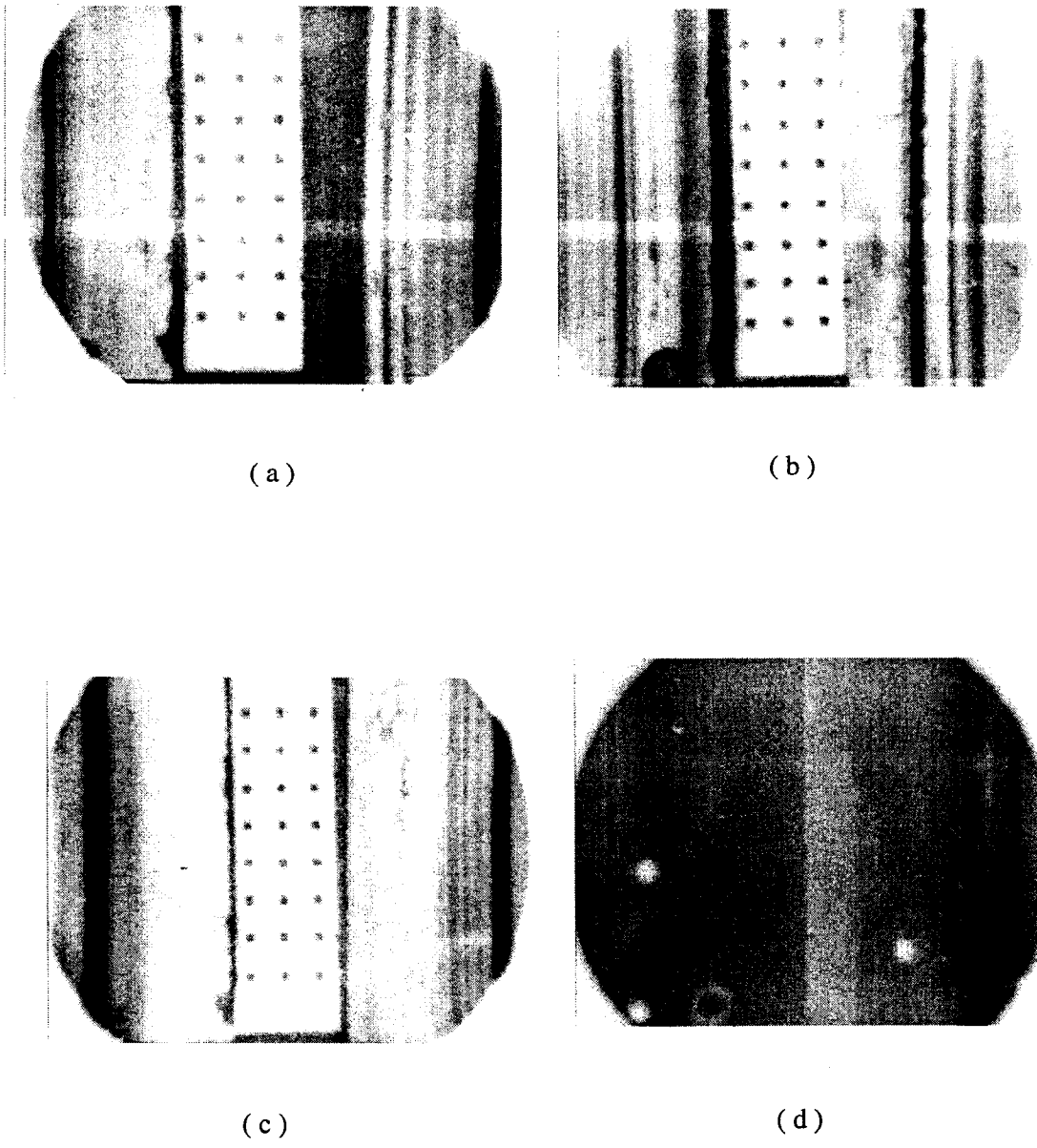

Figure 4. The four simultaneous images of the calibration grid, when placed at the origin of the coordinate system. (a) Image from the Center camera; (b) image from the Left camera; (c) image from the Right camera; and (d) image from the Shadow camera.

by AT&T Bell Laboratories, The University of Tennessee and Oak Ridge National Laboratory.

DGLSS is a least squares subroutine that solves undetermined or overdetermined systems oflinear equations, by performing a QR factorization of the input matrix, using Householder transformations. In matrix form, the system of equations to solve is

$$\begin{bmatrix} x_1 & y_1 & z_1 & 1 & 0 & 0 & 0 & 0 & -u_1x_1 & -u_1y_1 & -u_1z_1 \\ 0 & 0 & 0 & 0 & x_1 & y_1 & z_1 & 1 & -v_1x_1 & -v_1y_1 & -v_1z_1 \\ x_2 & y_2 & z_2 & 1 & 0 & 0 & 0 & 0 & -u_2x_2 & -u_2y_2 & -u_2z_2 \\ 0 & 0 & 0 & 0 & x_2 & y_2 & z_2 & 1 & -v_2x_2 & -v_2y_2 & -v_2z_2 \\ \cdot & \cdot & \cdot & \cdot & \cdot & \cdot & \cdot & \cdot & \cdot & \cdot & \cdot \\ \cdot & \cdot & \cdot & \cdot & \cdot & \cdot & \cdot & \cdot & \cdot & \cdot & \cdot \\ \cdot & \cdot & \cdot & \cdot & \cdot & \cdot & \cdot & \cdot & \cdot & \cdot & \cdot \\ \cdot & \cdot & \cdot & \cdot & \cdot & \cdot & \cdot & \cdot & \cdot & \cdot & \cdot \\ \cdot & \cdot & \cdot & \cdot & \cdot & \cdot & \cdot & \cdot & \cdot & \cdot & \cdot \\ \cdot & \cdot & \cdot & \cdot & \cdot & \cdot & \cdot & \cdot & \cdot & \cdot & \cdot \\ \cdot & \cdot & \cdot & \cdot & \cdot & \cdot & \cdot & \cdot & \cdot & \cdot & \cdot \\ \cdot & \cdot & \cdot & \cdot & \cdot & \cdot & \cdot & \cdot & \cdot & \cdot & \cdot \\ \cdot & \cdot & \cdot & \cdot & \cdot & \cdot & \cdot & \cdot & \cdot & \cdot & \cdot \\ \cdot & \cdot & \cdot & \cdot & \cdot & \cdot & \cdot & \cdot & \cdot & \cdot & \cdot \\ x_N & y_N & z_N & 1 & 0 & 0 & 0 & 0 & -u_Nx_N & -u_Ny_N & -u_Nz_N \\ 0 & 0 & 0 & 0 & x_N & y_N & z_N & 1 & -v_Nx_N & -v_Ny_N & -v_Nz_N \end{bmatrix} * \begin{bmatrix} t_{11} \\ t_{12} \\ t_{13} \\ t_{14} \\ t_{21} \\ t_{22} \\ t_{23} \\ t_{24} \\ t_{31} \\ t_{32} \\ t_{33} \end{bmatrix} = \begin{bmatrix} u_1 \\ v_1 \\ u_2 \\ v_2 \\ \cdot \\ \cdot \\ \cdot \\ \cdot \\ \cdot \\ \cdot \\ \cdot \\ \cdot \\ \cdot \\ \cdot \\ u_N \\ v_N \end{bmatrix}, \qquad [6]$$

with $N = 546$.

To the end of quantifying the effect κ, the system [4] and [5] was also solved. For this case the transformation parameters t_{ij}'s computed by DGLSS were used as initial guesses in the non-linear system, in which κ was initially set to zero. Then, the t_{ij}'s and κ were fed into the subroutine DNLS1E, which is a least squares subroutine that uses a modified Levenberg-Marquardt algorithm to solve N non-linear functions on M variables. DNLS1E is also part of NETLIB. DNLS1E requires the non-linear system to be input as an external function.

2.2.4. Calibration error

Once all the t_{ij}'s, and κ, were determined, an error analysis was performed. The final results are shown in table 1. Observe that the inclusion of κ did not affect the results, so it was decided to consider only with the equations [2] and [3], to simplify and accelerate calculations that would

Table 1. Camera calibration errors

error	Left camera		Center camera		Right camera	
[pixel]	DLT	DLT + κ $\kappa = -1.6\times10^{-12}$	DLT	DLT + κ $\kappa = -1.6\times10^{-12}$	DLT	DLT + κ $\kappa = -3.7\times10^{-12}$
rms u	1.2	1.2	1.0	1.0	1.4	1.4
max u	3.5	3.5	3.3	3.3	3.8	3.8
rms v	0.9	0.9	1.0	1.0	1.0	1.0
max v	2.8	2.8	3.2	3.2	5.5	5.5

be performed later. The null influence of κ was due, mainly, to the high value of the focal length (high zoom) of the telephoto lens. To better quantify the calibration error, it was necessary to compare the rms errors against the average area of a typical seed particle image. Such average value was about 40 pixel, and the minimum area for any image spot of a seed particle was 9 pixel. Then, if an image spot is considered as a square, the spot will have a side of 3 pixel, value that was higher than any of the rms errors, for any camera.

One of the major advantages in positioning the cameras on the chosen experimental set up was that the orthogonal cameras (Center and Shadow) would provide directly two out of the three world coordinates of the seed particles and/or the bubbles. The other two cameras would basically help on the estimation of the out of plane coordinate. To actually achieve such positioning it was necessary to prove that the v coordinates (z world coordinates) coincided on all the cameras, and that the image plane of the orthogonal cameras was parallel to the world plane they were seeing. The calibration results showed that the maximum difference between any camera, at any calibration point, for the v coordinates was less than 3 pixel, for the same world point, naturally. This maximum difference was between the center and the left cameras.

Also, for the Center camera, the maximum error in the X direction, on any calibration point, when moving the calibration grid in the Y direction, was less than 4 pixel. This happened at X = -1.27 mm. With respect the Z direction, the maximum error for any calibration point was less than 2 pixel. It is safe, then, to say that the image plane of the Center camera was parallel to the XZ plane. For the Shadow camera the results of calibration are very similar to those of the center

camera. In the Z direction, the maximum error was less than 2 pixel; and, in the Y direction the maximum error was less than 5 pixel. This maximum difference was at Y = -2.0 mm. Therefore, the Shadow camera image plane could be considered parallel to the YZ plane.

In all above cases, the calibration error was mainly due to the change of illumination on the calibration grid, when it moved to different positions. The calibration results, then, confirmed that the zoom of the telephoto lens was the same for all cameras, and that the desired positioning of the cameras was effectively achieved.